Journal of Computational Chemistry

WILEY

Journal of COMPUTATIONAL CHEMISTRY

RESEARCH ARTICLE OPEN ACCESS

Accuracy of Reaction Coordinate Based Rate Theories for Modelling Chemical Reactions: Insights From the Thermal Isomerization in Retinal

Simon Ghysbrecht[1] | Luca Donati[2,3] | Bettina G. Keller[1]

[1]Department of Biology, Chemistry and Pharmacy, Freie Universität Berlin, Berlin, Germany | [2]Department of Mathematics and Computer Science, Freie Universität Berlin, Berlin, Germany | [3]Modeling and Simulation of Complex Processes, Zuse Institute Berlin, Berlin, Germany

Correspondence: Bettina G. Keller (bettina.keller@fu-berlin.de)

Received: 17 July 2024 | **Revised:** 24 October 2024 | **Accepted:** 27 October 2024

Funding: This research has been funded by Deutsche Forschungsgemeinschaft (DFG) through grant SFB 1114 "Scaling Cascades in Complex Systems"–project number 235221301, as well as by the Cluster of Excellence MATH+, project AA1-15 "Math-powered drug-design". S.G. acknowledges funding by the Deutsche Forschungsgemeinschaft (DFG, German Research Foundation) under Germany´s Excellence Strategy – EXC 2008 – 390540038 – UniSysCat.

Keywords: diffusion | kramers | metadynamics | path collective variable | rate theory | retinal | square root approximation | umbrella sampling

ABSTRACT

Modern potential energy surfaces have shifted attention to molecular simulations of chemical reactions. While various methods can estimate rate constants for conformational transitions in molecular dynamics simulations, their applicability to studying chemical reactions remains uncertain due to the high and sharp energy barriers and complex reaction coordinates involved. This study focuses on the thermal cis-trans isomerization in retinal, employing molecular simulations and comparing rate constant estimates based on one-dimensional rate theories with those based on sampling transitions and grid-based models for low-dimensional collective variable spaces. Even though each individual method to estimate the rate passes its quality tests, the rate constant estimates exhibit considerable disparities. Rate constant estimates based on one-dimensional reaction coordinates prove challenging to converge, even if the reaction coordinate is optimized. However, consistent estimates of the rate constant are achieved by sampling transitions and by multi-dimensional grid-based models.

1 | Introduction

Elucidating chemical reaction mechanisms and rates is a central goal in computational chemistry. Yet, calculating this type of dynamical properties remains significantly more challenging than obtaining structural or thermodynamic information. Making precise predictions of reaction rates is particularly difficult.

The difficulties arise from two main sources: inaccuracies in the model of the potential energy surface (PES) [1], and inaccuracies in the method to calculate the rate on this PES [2]. Modeling a chemical reaction often requires a highly accurate PES based on explicitly evaluating the electronic structure at each nuclear configuration. Until recently, the computational cost of electronic structure methods has been so large that their use has been confined to single-point calculations [3] or short simulations of small systems [4]. Only a few rate theories can work with so little information. Among them Eyring transition state theory [5] remains the most frequently used method. However, several extensions of Eyring transition state theory, such as variational transition state theory [6, 7] and Grote-Hynes theory [8], have been introduced to account for recrossing and the influence of the solvent.

With recent advances in electronic structure methods [9, 10] and the advent of neural network potentials [11, 12], molecular dynamics (MD) simulations of chemical reactions in complex environments become possible, allowing for the explicit

treatment of solvent effects and entropic effects. A wide variety of methods to estimate rates [13, 14], that have been developed in the context of MD simulations of soft-matter systems, can now be applied to chemical reactions in complex environments. Soft-matter systems are characterized by rugged PES with multiple minima connected by energy barriers that are in the same range as the thermal energy. Examples are peptide [15] and protein dynamics [16], molecular binding [17] or crystal nucleation [18]. The accuracy of simulation-based rate estimates in the context of chemical reactions, which usually feature a single high and sharp barrier, is still a matter of debate.

It is important to acknowledge that simulation-based rate estimates are founded on classical mechanics and therefore do not account for quantum tunneling or energy quantization. While quantum tunneling is significant in proton transfer reactions, its rate diminishes exponentially with the square root of the reactant's mass and the barrier height. As a result, for reactions involving carbon or other medium-mass atoms, quantum tunneling is observable only when the reactant molecule is highly strained and consequently the reaction barrier is low [19]. However, energy quantization of the vibrational degrees of freedom does have a noticeable effect in most reactions, in particular, if the reactant molecule is rigid. For the thermal isomerization of protonated Schiff bases, which are closely related to retinal, neglecting the energy quantization incurs an error in the reaction rate of about a factor of three at room temperature [2]. It is worth noting that one can incorporate the effect of energy quantization into the potential energy and thereby achieve quantum-corrected classical dynamics [20].

Simulation-based rate estimates broadly fall into two distinct categories. The first approach is based on counting transitions across the reaction barrier. Since for most chemical reactions, the mean first passage time exceeds the accessible simulation time by far, one employs dynamical reweighting techniques, in which the sampling is enhanced and the transition count is subsequently reweighted [21–23]. Infrequent metadynamics [24] falls into this category.

The second approach is based on assuming an effective dynamics along a one-dimensional reaction coordinate, which requires the free energy surface and diffusion constant or diffusion profile as a function of this reaction coordinate. The influence of the neglected degrees of freedom and the curvature of the reaction coordinate on the system's dynamics are captured by these two functions, which can be readily estimated from atomistic simulations of the full molecular system [25–27]. From the effective dynamics, one may then derive analytical expressions for the rate constants. Kramers' rate theory [28, 29] falls into this second category.

The advantage of Kramers' theory is that, given a reaction coordinate, the individual steps of this approach are well-established and straight-forward. However, both the free energy surface and the diffusion constant depend on the reaction coordinate, and thus the accuracy of the rate estimate hinges on the quality of this coordinate.

Furthermore, Kramers' analytical expressions for the rate fall into three limiting cases (friction regimes), and it is essential to ensure the correct friction regime is applied. Both the barrier height and the "sharpness" of the barrier, represented by the barrier frequency, determine the friction regime. The high friction regime is induced by high barriers (compared to thermal energy) and broad barriers (barrier frequency compared to friction due to the implicit degrees of freedom). The low and intermediate friction regimes are induced by low and sharp barriers. Chemical reactions with high and sharp barriers fall into a middle ground, where it is not a priori clear whether the high friction regime applies.

To investigate how these effects play out in a chemical reaction, we study the thermal cis-trans isomerization around the $C_{13} = C_{14}$ double bond of retinal coupled to a lysine in vacuum [30, 31]. As PES, we use an empirical force field, whose computational efficiency permits a broad comparison of rate estimates. For a cis-trans isomerization, one may use an empirical force field, because the molecule's sigma bonds stay intact. Our goal is to explore whether classical MD in combination with Kramers' rate theory can model this reaction with quantitatively accurate reaction rates and mechanisms (on a given PES). As a comparison, we include rate estimates for overdamped Langevin dynamics along a one-dimensional reaction coordinate (Pontryagin's rate theory [32]), grid-based models [33, 34] of an effective dynamics in a multidimensional collective variable space, and infrequent metadynamics [24].

2 | Theory

2.1 | Definitions

The cis-trans isomerization of retinal is a unimolecular reaction

$$A \overset{k_{AB}}{\rightarrow} B \tag{1}$$

where A is the cis isomer, B is the trans isomer, and k_{AB} is the reaction rate constant. The rate constant is related to the mean first-passage time (MFPT) τ_{AB} by

$$k_{AB} = \frac{1}{\tau_{AB}} \tag{2}$$

The configuration of the molecule is given by the positions of its N atoms in Cartesian space: $\mathbf{x} \in \Gamma_x \subset \mathbb{R}^{3N}$, where Γ_x is called configuration space. We model the dynamics within the Born-Oppenheimer approximation, where $V(\mathbf{x})$ represents the Born-Oppenheimer potential energy of the electronic ground state. Reactant state $A \subset \Gamma_x$ and the product state $B \subset \Gamma_x$ are regions around minima in $V(\mathbf{x})$, whereas the transition state (TS) corresponds to a saddle point in $V(\mathbf{x})$.

Collective variables are low-dimensional representations of the $3N$-dimensional atomic positions. A collective variable vector is a (possibly non-linear) function

$$\mathbf{q} : \Gamma_x \rightarrow \mathbb{R}^m \tag{3}$$

which maps each position $\mathbf{x} \in \Gamma_x$ onto a low-dimensional vector $\mathbf{q} \in \mathbb{R}^m$, where $m \ll 3N$.

The free energy along $\mathbf{q}$ is defined as:

$$F(\mathbf{q}) = -RT\ln\pi(\mathbf{q}) \tag{4}$$

where $\pi(\mathbf{q})$ is the configurational Boltzmann density marginalized to the collective variable space

$$\pi(\mathbf{q}) = Z_{\text{conf}}^{-1}\int_{\Gamma_x} \mathrm{d}\mathbf{x}\, \exp\left(-\frac{V(\mathbf{x})}{RT}\right)\delta\left[\mathbf{q}(\mathbf{x}) - \mathbf{q}\right] \tag{5}$$

Here, $\delta\left[\mathbf{q}(\mathbf{x}) - \mathbf{q}\right]$ is the Dirac delta function and Z_{conf} is the configurational part of the classical partition function $Z_{\text{conf}} = \int_{\Gamma_x} \mathrm{d}\mathbf{x}\, \exp\left(-V(\mathbf{x})/RT\right)$.

A reaction coordinate is a one-dimensional collective variable that scales monotonously between reactant state A and product state B:

$$q : \Gamma_x \to [0,1] \tag{6}$$

q is zero for the reactant state A and one for the product state B. In this manner, q represents the progress of the reaction. Other intervals are also possible, but can be rescaled to $[0,1]$. The free energy $F(q)$ along the reaction coordinate is defined analogous to Equations (4) and (5).

In Equations (4) and (5), R is the ideal gas constant and T is the temperature. We calculate and report potential and free energies in units of J/mol, correspondingly the thermal energy is also reported as a molar quantity: RT. If units of energy are used for potential and free energies, R should be replaced by the Boltzmann constant $k_B = R/N_A$ in Equations (4) and (5) and all of the following equations. N_A is the Avogadro constant.

Equations of motion for the effective dynamics for q and $\mathbf{q}$ (underdamped Langevin dynamics, overdamped Langevin dynamics with and without position dependent diffusion), as well as the associated Fokker-Planck operators are reported in Section I of the Supporting Information.

The equations of motion for the effective dynamics require an effective mass (molar) μ_q, which can be estimated from the equipartition theorem [26]

$$\langle E_{\text{kin}} \rangle = \frac{1}{2}\mu_q \langle v^2 \rangle = \frac{1}{2}RT \tag{7}$$

where $\langle v^2 \rangle$ is the average squared velocity along q.

The rate theories introduced in the following, with the exception of the grid-based models, all assume separation of time scales. That is, on average, the system should fully sample the local equilibrium distribution within A, before it escapes over the transition state TS. This is only the case if the free energy barrier $F_{AB}^{\ddagger}$ of the reaction is much larger than the thermal energy: $F_{AB}^{\ddagger} \gg RT$.

2.2 | Simple Transition State Theory

In simple TST [13, 29] (or equivalently: harmonic TST or Vineyard TST), one uses a one-dimensional reaction coordinate q and the free energy $F(q)$ along this reaction coordinate. A then corresponds to the region around a minimum on the one-dimensional free energy surface, whereas TS is a point q_{TS} along the reaction coordinate that separates reactant state A ($q < q_{TS}$) and product state B ($q > q_{TS}$). Usually TS is positioned at the maximum of the free energy barrier. The rate is derived by considering the probability flux across TS (see Supporting Information Section I)

$$k_{AB} = \kappa \cdot \frac{\omega_A}{2\pi}\exp\left(-\frac{F_{AB}^{\ddagger}}{RT}\right) \tag{8}$$

The free energy barrier is

$$\begin{aligned} F_{AB}^{\ddagger} &= F(q_{TS}) - F(q_A) \\ F_{BA}^{\ddagger} &= F(q_{TS}) - F(q_B) \end{aligned} \tag{9}$$

where $F_{AB}^{\ddagger}$ is measured from the free energy minimum of A to TS, and, analogously, $F_{BA}^{\ddagger}$ is measured from the free energy minimum of B to TS. ω_A in Equation (8) is the angular frequency of the harmonic approximation of the reactant state minimum. $\kappa \in [0,1]$ is the transmission factor, which accounts for the fraction of molecules that proceed from TS to the product state B. Molecules, that revert to A after they have already passed TS, recross the transition state region. At this point, κ is an ad-hoc correction to the rate constant. In this contribution, we will set $\kappa = 1$ when applying Equation (8), meaning that all molecules that reach TS complete the reaction, and recrossing can be neglected.

2.3 | Kramers' Rate Theory

In Kramers' rate theory [28, 29], one uses a one-dimensional reaction coordinate q. One models the effective dynamics along q by underdamped Langevin dynamics, where the free energy $F(q)$ takes the role of the potential energy governing the drift and the neglected degrees act as a thermal bath. The interaction with this thermal bath is modeled by a friction and a random force, where the friction force can be scaled by a friction coefficient or collision rate ξ (with units time^{-1}). Thus, two thermal parameters enter Kramers' model: ξ and T.

One models $F(q)$ as a double well function, where the minima correspond to reactant (A) and product (B) states, and the barrier corresponds to the transition state (TS). Around each of the three states, $F(q)$ is approximated by a harmonic function

$$F(q) = \begin{cases} F(q_A) + \frac{1}{2}\mu_q\,\omega_A^2\left(q - q_A\right)^2 & \text{if } q \approx q_A \\ F(q_{TS}) - \frac{1}{2}\mu_q\,\omega_{TS}^2\left(q - q_{TS}\right)^2 & \text{if } q \approx q_{TS} \\ F(q_B) + \frac{1}{2}\mu_q\,\omega_B^2\left(q - q_B\right)^2 & \text{if } q \approx q_B \end{cases} \tag{10}$$

where q_A, q_B, and q_{TS} are positions of the extrema, ω_A, ω_B, and ω_{TS} are the angular frequencies of the harmonic approximation around the extrema. Figure 1a,c,e show the harmonic approximation for double wells on a circular coordinate.

In total, five parameters originating from the free energy surface govern Kramers' model: ω_A, ω_B, ω_{TS}, $F^{\ddagger}_{AB}$, and $F^{\ddagger}_{BA}$. To obtain the rate constant, the thermal parameters are compared to the free energy parameters. Three limiting cases are classified according to the thermal energy $RT/F^{\ddagger}_{AB}$ and the friction ξ/ω_{TS} (See fig. 15 in [29]).

The weak friction limit (or sometimes: diffusion-limited regime) is defined by $\xi/\omega_{TS} < RT/F^{\ddagger}_{AB}$. In this regime, the deterministic forces (due to the free energy) dominate the diffusive forces (friction and the thermal noise terms). Thus, the underdamped Langevin dynamics is quasi-Hamiltonian. The rare interactions with the heat bath cause the total energy of the system to slowly oscillate, and the rate constant is derived by considering the time evolution for the energy probability density [29]. One obtains

$$k_{AB} = \frac{I(F^{\ddagger}_{BA})}{I(F^{\ddagger}_{AB}) + I(F^{\ddagger}_{BA})} \cdot \xi \frac{I(F^{\ddagger}_{AB})}{RT} \cdot \frac{\omega_A}{2\pi} \exp\left(-\frac{F^{\ddagger}_{AB}}{RT}\right) \tag{11}$$

where

$$\begin{aligned} I(F^{\ddagger}_{AB}) &= \oint_{H(q,p)=F^{\ddagger}_{AB}} p \, \mathrm{d}q \\ &= 2\int_{q^-_{AB}}^{q^+_{AB}} \sqrt{2\mu_q\left(F^{\ddagger}_{AB} - F(q)\right)} \, \mathrm{d}q \\ &= \frac{2\pi F^{\ddagger}_{AB}}{\omega_A} \end{aligned} \tag{12}$$

is an integral over closed orbits of the phase space corresponding, respectively to the total energy $F^{\ddagger}_{AB}$. $I(F^{\ddagger}_{BA})$ is defined analogously. The limits of the integrals are obtained by setting $p = 0$ in the Hamiltonian function: $q^{\pm}_{AB} = q_A \pm \sqrt{2F^{\ddagger}_{AB}/\mu_q\omega_A^2}$ (and equivalent $q^{\pm}_{BA} = q_B \pm \sqrt{2F^{\ddagger}_{BA}/\mu_q\omega_B^2}$). The resulting formula is the reduced action of the harmonic oscillator at an energy $F^{\ddagger}_{AB}$ (and equivalent for $F^{\ddagger}_{BA}$). A sharp peak at the transition state corresponds to a large value of ω_{TS}, and thus might induce the weak friction limit.

The moderate-to-high friction limit is defined by $\xi/\omega_{TS} > RT/F^{\ddagger}_{AB}$. The diffusive forces are stronger than the deterministic forces, but not by orders of magnitude. In this regime, one assumes a steady state probability flux from state A across the transition state region [29]. This assumption replaces the requirement for thermal equilibrium between reactant and transition state in transition state theory. This yields

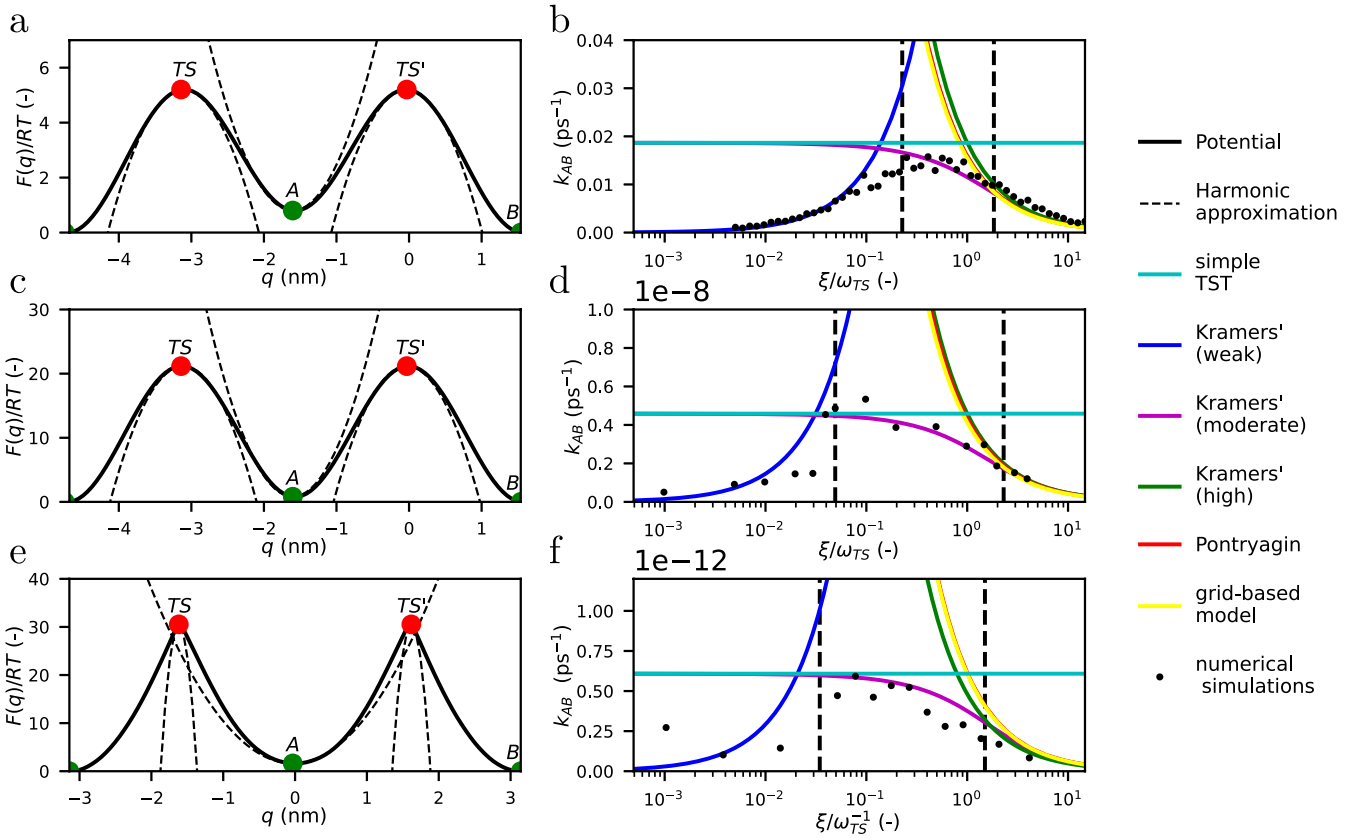

FIGURE 1 | One-dimensional model systems and corresponding rate constants from A to B as a function of ξ/ω_{TS}: (a,b) low barriers; (c,d) high and broad barriers; (e,f) high and sharp barriers. Rates have been calculated by simple TST (Equation 8), Kramers' weak friction (Equation 11), Kramers' moderate friction (Equation 13), Kramers' high friction (Equation 14), Pontryagin (Equation 16), grid-based model (Equation 18), and from numerical simulations. The Threshold between weak and moderate friction is $\xi/\omega_{TS} = RT/F^{\ddagger}_{AB}$. Threshold between moderate and high friction is at the value of ξ/ω_{TS} where Equations (13) and (14) deviate less than five percent.

$$k_{AB} = \frac{\xi}{\omega_{TS}}\left(\sqrt{\frac{1}{4}+\frac{\omega_{TS}^2}{\xi^2}}-\frac{1}{2}\right)\cdot\frac{\omega_A}{2\pi}\exp\left(-\frac{F_{AB}^{\ddagger}}{RT}\right). \tag{13}$$

The high friction limit is defined by $\xi/\omega_{TS} \gg RT/F_{AB}^{\ddagger}$. The diffusive forces dominate the deterministic forces. At high values of ξ, the prefactor in Equation (13) can be approximated as ω_{TS}/ξ (see Supporting Informatiom Section I), yielding

$$k_{AB} = \frac{\omega_{TS}}{\xi}\cdot\frac{\omega_A}{2\pi}\exp\left(-\frac{F_{AB}^{\ddagger}}{RT}\right) \tag{14}$$

This regime is also called the spatial diffusion limited regime, or the diffusive regime.

The rate constants for the three friction regimes (Equations (11), (13), (14)) have the same functional form as in simple TST (Equation (8)), but in addition they provide explicit expressions for the transmission factor κ. Kramers' rate theory provides a model for recrossing in terms of the shape of the free energy surface, the temperature, and the strength of the heat bath.

2.4 | Pontryagin's Rate Theory

The following rate model is often quite generically introduced as a means to calculate the mean first-passage time (MFPT) τ_{AB} or escape rate k_{AB} for diffusion over a barrier. It is derived from the Fokker-Planck equation for overdamped Langevin dynamics (Smoluchowski equation). Here, we will refer to it as the Pontryagin's rate theory [32].

In Pontryagin's rate theory [29, 32], one uses a one-dimensional reaction coordinate q and models the effective dynamics along q by overdamped Langevin dynamics, which is the high friction limit of underdamped Langevin dynamics. In this rate theory, the friction coefficient $\xi(q)$ may vary along the reaction coordinate q. This generalization is important because the fluctuations of the neglected degrees of freedom may vary along q [27], and additionally the curvature of q may give rise to a position dependent friction. Conventionally, Pontryagin's rate constant is not formulated in terms of $\xi(q)$ but in terms of the closely related position dependent diffusion profile

$$D(q) = \frac{RT}{\mu_q \xi(q)} \tag{15}$$

where μ_q is a molar mass. The rate constant is then given by the following nested integral:

$$k_{AB} = \left\{\int_{q_A}^{q_B} dq' \left[\frac{1}{D(q')} e^{\beta F(q')} \int_{-\infty}^{q'} dq''\, e^{-\beta F(q'')}\right]\right\}^{-1} \tag{16}$$

with $\beta = 1/RT$. A closed-form version is not available, but computing the nested integral numerically is straightforward.

This expression for the rate constant does not make any assumptions on the shape of the reactant state and transition barrier and includes the full position dependent diffusion profile. Inserting the harmonic approximation and assuming constant diffusion in Equation (16) yields Kramers' rate equations in the high friction limit (Equation (14)).

2.5 | Grid-Based Models

In grid-based models [33, 34], one uses a multidimensional collective variable $\mathbf{q} \in \mathbb{R}^m$ and models the effective dynamics in this collective variable space by overdamped Langevin dynamics with position dependent diffusion. The collective variable space is discretized into n disjoint cells. The cells are divided into three sets $\mathcal{A}$, $\mathcal{B}$, and $\mathcal{I}$, where $\mathcal{A}$ represents the reactant state A, $\mathcal{B}$ represents the product state B, and $\mathcal{I}$ the intermediate region. Independent of the assignment to the three sets, the transition rate Q_{ij} from cell i to cell j is

$$Q_{ij} = \begin{cases} Q_{ij} & \text{if } i \neq j \text{ and cells adjacent} \\ 0 & \text{if } i \neq j \text{ and cells not adjacent} \\ -\sum_{l=1, l\neq i}^{n} Q_{il} & \text{if } i = j \end{cases}. \tag{17}$$

Equation (17) defines a $n \times n$ row-normalized rate matrix $\mathbf{Q}$ with elements Q_{ij}. $\mathbf{Q}$ is a discretization of the Fokker-Planck operator for overdamped Langevin dynamics, where we assumed that the free energy is constant within each grid cell.

Q_{ij} between adjacent cells can be calculated as [33–35]

$$Q_{ij} = D_{ij}\frac{S_{ij}}{\mathcal{V}_i h_{ij}}\cdot\frac{\sqrt{\pi(\mathbf{q}_j)\pi(\mathbf{q}_i)}}{\pi(\mathbf{q}_i)} \tag{18}$$

where $\mathbf{q}_i$ and $\mathbf{q}_j$ are the centers of the adjacent grid cells, $\pi(\mathbf{q})$ is given by Equation (5), $h_{ij} = \|\mathbf{q}_j - \mathbf{q}_i\|$ is the Euclidean distance between the centers of the cells, S_{ij} is the area of the intersecting surface between cells i and j, $\mathcal{V}_i$ is the volume of the Voronoi cell i, and D_{ij} is the diffusion on the boundary between cells i and j, which we approximate as $D_{ij} = \frac{1}{2}\left(D(\mathbf{q}_i) + D(\mathbf{q}_j)\right)$. Because of the square root in Equation (18), the approach is called the Square Root Approximation of the Fokker–Planck equation (FP-SqRA) [33, 34].

In Equation (18), the probability density at the cell boundary between adjacent cells is approximated by the geometric mean of the Boltzmann weights of the cells [33, 34]. Using a harmonic mean instead leads to the Harmonic Averaging Approximation of the Fokker-Planck equation (FP-HAA):

$$Q_{ij} = D_{ij}\frac{S_{ij}}{\mathcal{V}_i h_{ij}}\cdot\frac{1}{\pi(\mathbf{q}_j)}\frac{2\pi(\mathbf{q}_j)\pi(\mathbf{q}_i)}{\pi(\mathbf{q}_i)+\pi(\mathbf{q}_j)} \tag{19}$$

and has improved convergence properties [36].

Mean first-passage times $\tau_{i\to B}$ from any cell i to the product state B can be computed by solving [37]

$$\mathbf{Q}\,\boldsymbol{\tau}_B = -\mathbf{1} \tag{20}$$

for $\boldsymbol{\tau}_B = \left[\tau_{1\to B}, \ldots, \tau_{n\to B}\right]^T$. This vector contains MFPTs for all cells i to the product state B. To enforce this, Equation (20) must

be solved while imposing the boundary condition that $\tau_{k\to B} = 0$ for all $k \in \mathcal{B}$. The MFPT from A to B is then obtained by averaging over the state-wise MFPTs

$$\tau_{AB} = \sum_{i\in\mathcal{A}} \pi_{A,i}\tau_{i\to B} \tag{21}$$

where $\pi_{A,i} = \pi_i / \sum_{i\in\mathcal{A}}\pi_i$ and $\pi_i = \int_{\mathbf{q}\in\text{cell }i} \mathrm{d}\mathbf{q}\ \pi(\mathbf{q})$. The rate constant is the inverse of this MFPT (Equation (2)).

2.6 | Rates From Sampling Transitions

The system is simulated on $V(\mathbf{x})$, and the reaction rate k_{AB} is obtained as a statistical estimate of the observed transitions between A and B. It is sufficient to define $A \subset \Gamma_x$ and $B \subset \Gamma_x$ as regions in the configurational space; a transition state does not need to be defined. The first-passage times from A to B are recorded in a series of n simulations, whose initial states are located in A and which are terminated once they reach B. This yields a series of first-passage times $(\tau_{AB,1}, \tau_{AB,2} \ldots \tau_{AB,n})$.

The MFPT τ_{AB} can be calculated as the arithmetic mean of these first-passage times, or—with better statistical accuracy—by fitting the cumulative distribution function of a Poisson process [15]

$$P(\tau_{AB,i}) = 1 - \exp\left(-\frac{\tau_{AB,i}}{\tau_{AB}}\right) \tag{22}$$

to the cumulative distribution histogram of these first passage times. In Equation (22), τ_{AB} is the MFPT and acts as a fitting parameter, which is inserted into Equation (2) to obtain the reaction rate.

For reactions with high energy barriers, the transition times are orders of magnitude longer than the accessible simulation times. Therefore, in infrequent metadynamics simulations [24, 38], a time-dependent bias function $U(\mathbf{x}, t)$ is introduced that increases in strength as the simulation proceeds and pushes the system over the barrier into state B. Each accelerated first-passage time is then reweighted to the corresponding physical first-passage time by a discretized time-integral over the length of the trajectory [24, 39, 40]

$$\tau_{AB,i} = \Delta t \sum_{k=1}^{T_i} \exp\left(\frac{U(\mathbf{x}_{i,k}, k\Delta t)}{RT}\right) \tag{23}$$

where Δt is the time step of the trajectory, T_i is the total number of time steps in the ith trajectory, $\mathbf{x}_{i,k}$ is the kth configuration in this trajectory, and $t = k\Delta t$ is the corresponding time. This reweighting assumes that no bias has been deposited on the transition state, which is approximately ensured by the slow deposition of the infrequent metadynamics protocol.

3 | Results

3.1 | Friction Regimes

To study the effect of the curvature of the free energy surface on the friction regime independently from the choice of the reaction coordinate, we devised one-dimensional model systems with a circular reaction coordinate $q \in [-\pi, +\pi]$. As in the actual retinal molecule, the free energy functions $F(q)$ for these models exhibits two energy barriers and two minima. The models differ in the height and the "sharpness" of the barriers, where the first model has low and broad free energy barriers, the second model has high and broad free energy barriers. The third model is the actual free energy function along the $C_{13} = C_{14}$ torsion angle of retinal and exhibits sharp and high free energy barriers. Figure 1a,c,e show the free energy functions along with the harmonic approximations for the minima and the barriers. Table 1 reports the corresponding parameters. We set $T = 300$ K, and thus the thermal energy is $RT = 2.49\ \text{kJ mol}^{-1}$.

TABLE 1 | Parameters for one-dimensional rate theories calculated for the one-dimensional systems.

		Small barrier	High barrier	Inter-polated	
				TS	*TS′*
RT	kJ mol^{-1}	2.49	2.49	2.49	
$F^{\ddagger}_{AB}$	kJ mol^{-1}	10.98	50.84	72.11	72.10
$F^{\ddagger}_{BA}$	kJ mol^{-1}	12.96	52.74	76.15	76.14
ω_A	ps^{-1}	4.78	10.13	6.83	
ω_B	ps^{-1}	4.98	10.21	7.60	
ω_{TS}	ps^{-1}	4.89	10.17	48.38	46.21
Energy ratio					
$RT/F^{\ddagger}_{AB}$	—	0.23	0.05	0.03	0.03
Threshold between weak and moderate friction					
ξ/ω_{TS}	—	0.23	0.05	0.03	0.03
ξ	ps^{-1}	1.12	0.51	1.45	1.39
Threshold between moderate and high friction					
ξ/ω_{TS}	—	1.90	2.30	1.50	1.57
ξ	ps^{-1}	9.29	23.39	72.57	72.55

With increasing barrier height, the rate constant due to simple TST drops by orders of magnitude from $k_{AB} \sim 10^{-2}$ps to $k_{AB} \sim 10^{-9}$ps and $k_{AB} \sim 10^{-13}$ps (cyan lines in Figure 1b,d,f). However, comparison to the numerical simulations (black dots in Figure 1b,d,f) shows that simple TST is a crude approximation and severely overestimates the rate constants in the low and high friction regimes.

The numerical simulations reproduce Kramers' turnover [29, 41], i.e., the bell curve characterized by low rates in the weak friction regime, high rates in the moderate friction region, and low rates again in the high friction region (see Supporting Information Table S.7 for representative numerical values). Kramers' rate theory models this turnover by devising a separate rate equation for each of the three friction regimes (Equations (11), (13), and (14)). The theory requires that $F^{\ddagger}_{AB} \gg RT$, which is well fulfilled for

the second ($F^{\ddagger}_{AB} = 20.4\ RT$) and the third model ($F^{\ddagger}_{AB} = 29.0\ RT$) and to a lesser extent for the first model ($F^{\ddagger}_{AB} = 4.4\ RT$).

The friction regime is determined by the relative sizes of the ratios $RT/F^{\ddagger}_{AB}$ and ξ/ω_{TS}. The ratio $RT/F^{\ddagger}_{AB}$ compares the thermal energy to the free energy barrier. Within the assumptions of Kramers' theory, $RT/F^{\ddagger}_{AB} \ll 1$. The ratio ξ/ω_{TS} compares the time it takes to cross the transition state region, $1/\omega_{TS}$, to the average time between two interactions with the thermal bath. $\xi/\omega_{TS} > 1$ means that, on average, several interactions with the thermal bath occur while the system crosses the transition state region, implying a high friction regime. $\xi/\omega_{TS} < 1$ means that, on average, no interaction with the thermal bath occurs while the system crosses the transition state region, implying a weak friction regime. For $\xi/\omega_{TS} \approx 1$, transition time and interaction with the thermal bath occur on the same timescale.

All other parameters being equal, an increase in the curvature of the free energy barrier leads to an increase in ω_{TS} and thus might shift the effective dynamics into the weak or intermediate friction regime. In our model systems, the ω_{TS} increases across the models from $\omega_{TS} \approx 5\ \mathrm{ps}^{-1}$ to $\omega_{TS} \approx 10\ \mathrm{ps}^{-1}$ and finally reaching $\omega_{TS} = 48.38\ \mathrm{ps}^{-1}$, and $\omega_{TS'} = 46.21\ \mathrm{ps}^{-1}$ for the model representing the actual retinal. Simultaneously, the free energy barrier increases across the models. The resulting boundaries between the friction regimes are shown as vertical dashed lines in Figure 1b,d,f.

Kramers' rate constants k_{AB} as a function of ξ/ω_{TS} are represented as blue, purple, and green lines for the three friction limits (Figure 1b,d,f). Each of the three rate equations agrees well with the numerical results when applied within the appropriate friction regime. Outside of their respective friction regime, the three rate equations yield very inaccurate results. In particular, the rate equation for the high friction regime vastly overestimates the rates in the weak and moderate friction regime.

Additionally, we report the results from Pontryagin's rate theory (red line, Equation (16)) and the grid-based model (yellow line, Equation (18)), which both assume overdamped Langevin dynamics. For a position independent friction coefficient ξ, these models closely align with the high friction regime of Kramers' rate theory, and equally overestimate the rate constant in the weak and moderate friction regime. These results underline the importance of determining the system's friction regime and choosing the appropriate rate model.

For the free energy function of retinal (third model system), the moderate friction regime ranges from $\xi = 1.45\ \mathrm{ps}^{-1}$ to $\xi = 72.57\ \mathrm{ps}^{-1}$. The friction coefficient ξ of the effective dynamics along q is not a parameter that can be chosen freely, but it is determined by the influence of the neglected degrees of freedom and is calculated from the diffusion constant $D(q)$ (Equation (15)) and the effective mass μ_q (Equation (7)). This is explored in the following section.

3.2 | Atomistic Model of Retinal

Our model of retinal (Figure 2a) consists of the retinal molecule, which is covalently bound to a capped lysine residue via a protonated Schiff base [42]. This corresponds to the chemical structure of retinal in a protein environment. Since the lysine residue cannot move freely in a protein environment, we placed position restraints on all heavy atoms of lysine (backbone and side chain) as well as on the atoms in the caps. All atoms in retinal, including the cyclohexene ring were allowed to move freely. As a potential energy function of this molecule, we use an empirical atomistic force field. Our goal is to calculate the reaction rate constants of the thermal cis-trans isomerization around the $C_{13} = C_{14}$ double bond (Figure 2b,c), where the cis-configuration is the reactant state A and the trans-configuration is the product state B.

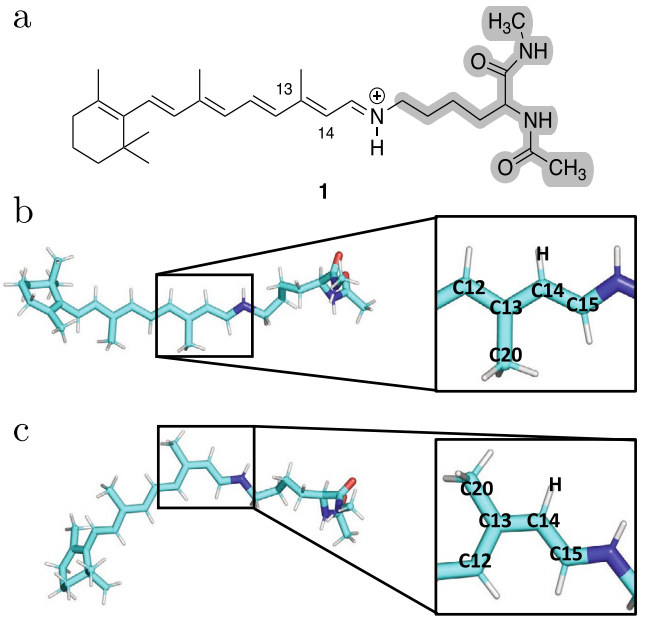

FIGURE 2 | (a) Retinal covalently linked to a capped lysine residue. Position restraints have been applied to heavy atoms highlighted in gray. (b) trans-configuration. (c) cis-configuration.

3.3 | $C_{13} = C_{14}$-Torsion Angle as Reaction Coordinate

As an initial reaction coordinate for the one-dimensional rate models, we choose the torsion angle φ constituted by the chain of carbon atoms C_{12}-$C_{13} = C_{14}$-C_{15} (Figure 2). Figure 3 shows two free energy functions along this reaction coordinate, which were numerically calculated by well-tempered metadynamics simulations [38] (blue line) and by umbrella sampling simulations [43] combined with weighted histogram analysis [44] (orange line). The statistical uncertainty of the free energy profiles are shown as shaded areas in Figure 3, but they are only about as large as the linewidth. The figure also shows the position dependent diffusion $D(\varphi)$ obtained from umbrella sampling simulations following [27]. Because of the sharp barriers, the diffusion profile could not be estimated in the transition regions, and we relied on the interpolation (dotted line in Figure 3) in these regions.

Both $F(\varphi)$ have minima at the cis-configuration ($\varphi = 0$ rad) and at the trans-configuration ($\varphi = \pm\pi$ rad), where we set the trans state to $F(\varphi) = F(\pi) = 0$. Cis- and trans-configurations have the same free energy in $F(\varphi)$ from umbrella sampling,

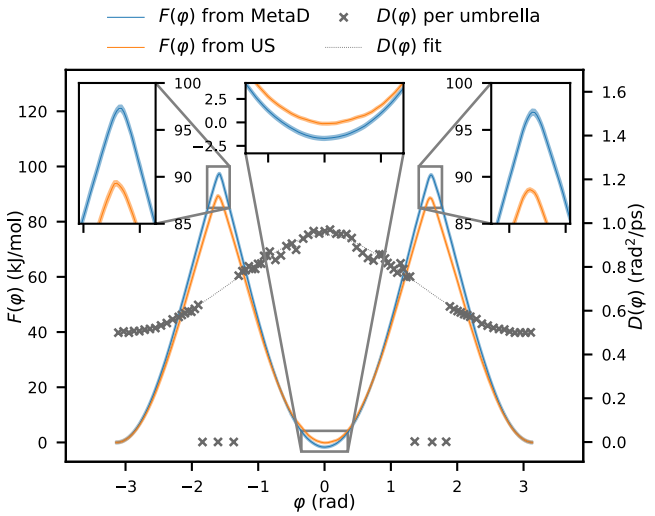

FIGURE 3 | Free energy surfaces $F(\varphi)$ and diffusion profiles $D(\varphi)$ estimated from umbrella sampling (US) and metadynamics (MetaD) by biasing the $C_{13} = C_{14}$ torsion angle φ. Statistical standard errors are given by the thickness of the curves.

whereas, in $F(\varphi)$ from metadynamics, the cis-configuration is about $1.6\ \text{kJ mol}^{-1}$ lower than the trans-configuration. The minima are separated by two free energy barriers TS and TS' corresponding to rotating clockwise and counterclockwise around φ, respectively. Both methods, umbrella sampling and metadynamics, predict that the barriers TS and TS' are equal in height. Umbrella sampling yields a barrier height of $F^{\ddagger}_{\text{cis}\to\text{trans}} = 89\ \text{kJ mol}^{-1}$, whereas metadynamics yields barriers that are about $10\ \text{kJ mol}^{-1}$ higher ($F^{\ddagger}_{\text{cis}\to\text{trans}} = 99\ \text{kJ mol}^{-1}$).

Even though we monitored the convergence of the two free energy methods carefully, the difference in the predicted free energy barrier is sizeable. At room temperature, the difference corresponds to about four times the thermal energy of $RT = 2.49\ \text{kJ mol}^{-1}$, and in absolute terms it is well above the limit for chemical accuracy of $1\ \text{kcalmol}^{-1} = 4.2\ \text{kJ mol}^{-1}$. Because the free energy difference enters exponentially in each of the rate models, this difference strongly affects the predicted rate. We return to this discussion in Section 3.6, but for now we will discuss rates based on the umbrella sampling $F(\varphi)$. The parameters for the one-dimensional rate theories for $F(\varphi)$ from umbrella sampling and from metadynamics are reported in Supporting Information Tables S.1 and S.2.

Next, we determine the friction regime by comparing the energy ratio is $RT/F^{\ddagger}_{\text{cis}\to\text{trans}} = 0.028$ to the friction ratio ξ_{TS}/ω_{TS}. The friction coefficient of the effective dynamics along φ is $\xi_{TS} = 132\ \text{ps}^{-1}$ for transitions via TS (determined via Equations (15) and (7)). The curvature of TS is $\omega_{TS} = 244\ \text{ps}^{-1}$, yielding the friction ratio $\xi_{TS}/\omega_{TS} = 0.54$. The corresponding ratio for the other barrier is $\xi_{TS'}/\omega_{TS'} = 0.50$. Both friction ratios are much higher than the energy ratio, and therefore the effective dynamics along φ fall into the moderate-to-high or even high friction regime.

Table 2 shows the rate constants derived from one-dimensional rate theories for the moderate and high friction regime. Methods that assume high friction (Kramers' (high friction), Pontryagin, grid-based) all yield a rate constant of $k_{\text{cis}\to\text{trans}} \approx 0.009 - 0.015\ \text{s}^{-1}$ for the cis-trans transition. The two methods that are based on overdamped Langevin dynamics (Pontryagin and grid-based models) yield indistinguishable rate constants ($k_{\text{cis}\to\text{trans}} \approx 0.009\ \text{s}^{-1}$), which is slightly lower than the high friction limit of Kramers' rate theory ($k_{\text{cis}\to\text{trans}} \approx 0.015\ \text{s}^{-1}$).

The high friction Kramers' rate constant ($k_{\text{cis}\to\text{trans}} \approx 0.015\ \text{s}^{-1}$) is higher than the one form the moderate friction regime ($k_{\text{cis}\to\text{trans}} \approx 0.006\ \text{s}^{-1}$). Since the two methods would coincide in the high friction region, this indicates, that the effective dynamics along φ fall into the moderate friction regime and are best described by Kramers' rate theory for moderate friction.

Simple TST is a reasonable approximation in the moderate friction regime and yields a rate constant of $k_{\text{cis}\to\text{trans}} \approx 0.008\ \text{s}^{-1}$, only slightly overestimating Kramers' rate constant for moderate friction. The rate constant of the reverse reaction, $k_{\text{trans}\to\text{cis}}$, are reported in Table 2 and shows the same effects.

3.4 | Comparison to Infrequent Metadynamics

Even though the results from one-dimensional rate theories (using φ as a reaction coordinate) seem consistent, they deviate drastically from rate constants estimated from molecular simulations (Table 2). We used infrequent metadynamics and biased along φ to simulate the cis-trans isomerization. The resulting rate constant, $k_{\text{cis}\to\text{trans}} = 2.23 \cdot 10^{-5}\ \text{s}^{-1}$, is more than two orders of magnitude smaller than the most appropriate one-dimensional rate theory $k_{\text{cis}\to\text{trans}} = 5.83 \cdot 10^{-3}\ \text{s}^{-1}$ (Kramers' with moderate friction). By moving from a one-dimensional system (Figure 1) to a high-dimensional system (Figure 2) we have lost the agreement between one-dimensional rate theories and numerical simulations.

The deviation between Kramers' rate theory and numerical simulation for retinal is in stark contrast to the good agreement between the two approaches for the one-dimensional systems. It is, however, in line with the results from [48], where we found a similar disparity between simulated rate constants and the moderate friction limit of Kramers' rate theory.

Two known error sources of infrequent metadynamics are (*i*) slow processes that occur orthogonal to the biased coordinate, e.g., due to sub-minima in the reactant state [45, 46], and (*ii*) perturbation of the transition state region because bias is deposited there [15, 24]. Retinal is a very rigid molecule and does not exhibit sub-minima within the cis- or within the trans-configuration, making the first error source unlikely. Our rate constants are insensitive to the variations in the bias deposition rate, which confirms that the transition state region is unperturbed (Figure S.4). Thus, for this specific system, the limitations of infrequent dynamics metadynamics do not explain the deviation results of one-dimensional rate theories.

A second error source might be a wrong choice of the friction regime. However, the analysis in Section 3.3 shows that, for this system, the difference between the high friction and

TABLE 2 | Rate constants determined through different methodologies for the thermal cis-trans isomerization over the $C_{13} = C_{14}$ double bond in retinal. (. . .): results sensitive to the grid.

			$F(q)$ via US		$F(q)$ via MetaD	
Method	**Equation**	**CV**	$k_{trans\to cis}$ [s^{-1}]	$k_{cis\to trans}$ [s^{-1}]	$k_{trans\to cis}$ [s^{-1}]	$k_{cis\to trans}$ [s^{-1}]
$C_{13} = C_{14}$-torsion angle as reaction coordinate						
Simple TST	(8)	φ	5.17×10^{-3}	7.55×10^{-3}	2.05×10^{-4}	1.60×10^{-4}
Kramers (moderate friction)	(13)	φ	3.99×10^{-3}	5.83×10^{-3}	1.67×10^{-4}	1.30×10^{-4}
Kramers (high friction)	(14)	φ	9.90×10^{-3}	1.45×10^{-2}	4.96×10^{-4}	3.86×10^{-4}
Pontryagin	(16)	φ	1.08×10^{-2}	8.93×10^{-3}	4.68×10^{-4}	2.17×10^{-4}
Grid-based	(19)	φ	1.07×10^{-2}	8.95×10^{-3}	4.67×10^{-4}	2.17×10^{-4}
Optimized reaction coordinate σ_s						
Simple TST	(8)	Path	2.41×10^{-4}	2.57×10^{-4}	9.56×10^{-6}	1.19×10^{-5}
Kramers (moderate friction)	(13)	Path	4.45×10^{-5}	4.81×10^{-5}	1.85×10^{-6}	2.26×10^{-6}
Kramers (high friction)	(14)	Path	4.61×10^{-5}	4.98×10^{-5}	1.92×10^{-6}	2.34×10^{-6}
Pontryagin	(16)	Path	5.80×10^{-5}	3.66×10^{-5}	2.51×10^{-6}	1.73×10^{-6}
Grid-based	(19)	Path	5.78×10^{-5}	3.66×10^{-5}	2.53×10^{-6}	1.75×10^{-6}
Grid-based model for multidimensional collective variables						
Grid-based (diffusion *grid1*)	(19)	φ, χ_1, χ_2	(5.66×10^{-6})	(7.05×10^{-6})	8.13×10^{-6}	1.23×10^{-5}
Grid-based (averaged *grid1*)	(19)	φ, χ_1, χ_2	(1.14×10^{-5})	(1.44×10^{-5})	1.58×10^{-5}	2.40×10^{-5}
Grid-based (diffusion *grid2*)	(19)	φ, χ_1, χ_2	(7.14×10^{-6})	(9.05×10^{-6})	1.03×10^{-5}	1.56×10^{-5}
Grid-based (averaged *grid2*)	(19)	φ, χ_1, χ_2	(1.02×10^{-5})	(1.35×10^{-5})	1.40×10^{-5}	2.13×10^{-5}

Sampling				
Method	**Equation**	**CV**	$k_{trans\to cis}$ [s^{-1}]	$k_{cis\to trans}$ [s^{-1}]
InMetaD	(23)	φ	2.18×10^{-5}	2.23×10^{-5}
InMetaD	(23)	φ, χ_1, χ_2	2.22×10^{-5}	2.60×10^{-5}

the intermediate friction results are small and do not explain the discrepancy with the simulation results. Specifically, high friction: $k_{cis\to trans} = 1.45\cdot10^{-2}\ s^{-1}$, moderate friction: $k_{cis\to trans} = 5.83\cdot10^{-3}\ s^{-1}$,simulation:$k_{cis\to trans} = 2.23\cdot10^{-5}\ s^{-1}$.

We conclude that the disparity between Kramers rate constant for moderate friction and the simulated results is based in the high-dimensionality of the system. One-dimensional rate theories are sensitive to the choice of reaction coordinate [47]. To explain the gap between the simulated rate constant and Kramers' rate constant, we will next optimize the reaction coordinate.

3.5 | Optimized Reaction Coordinate

The reaction coordinate $q = \varphi$ cleanly separates the reactant and the product state and thus fulfills an important criterion for a good reaction coordinate. However, closer inspections show that other degrees of freedom besides the torsion angle participate in the cis-trans isomerization. The bonding environments around C_{13} and C_{14} are planar when retinal is in the cis- or trans-configuration, but both C_{13} and C_{14} bend out of plane in the vicinity of the transition state [2, 48]. The out-of-plane motion around C_{13} is captured by the improper dihedral defined by $\{C_{13}, C_{14}, C_{12}, C_{20}\}$. Likewise, the out-of-plane motion around C_{14} is captured by the improper dihedral χ_2 defined by $\{C_{14}, C_{15}, C_{13}, H\}$. The correlation between φ and the two improper dihedrals has been demonstrated at the levels of DFT/B3LYP and DFTB [2, 48], and is also captured by our umbrella sampling simulations using an empirical force field.

Figure 4a shows the configurations of a series of umbrella sampling simulations projected into the two-dimensional space spanned by φ and χ_1. These distributions seem to "jump" at the transition states ($\varphi = \pm\frac{\pi}{2}$). The projection into the space spanned by φ and χ_2 shows a similar behavior (Figure 4b). Note that the amplitude of the "jump" is not very large, only ±0.4 rad, compared to the range of φ itself (in Supporting Information Figure S.5 the zoom on χ_1 and χ_2 has been removed to give a more realistic impression of the amplitude).

We optimized nonlinear reaction paths $\mathbf{s}(\sigma_s)$ in the space spanned by φ, χ_1, and χ_2 using the path-finding algorithm from

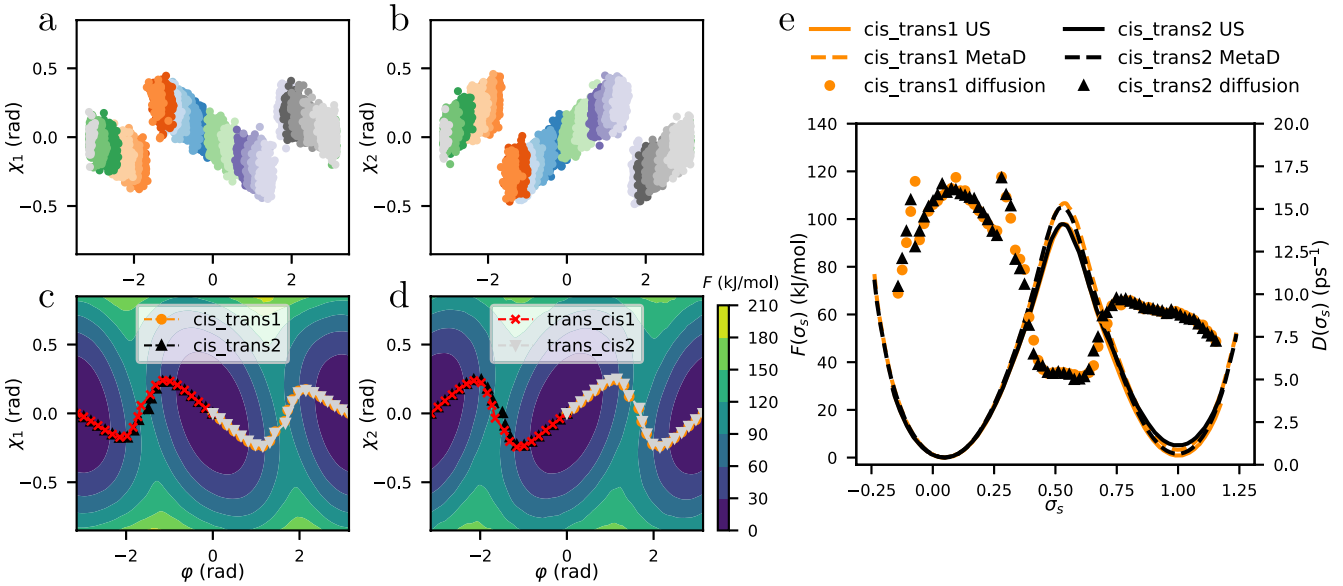

FIGURE 4 | (a) Scatter plots of the umbrella sampling simulations (one color per umbrella) for dihedral φ vs. improper dihedral χ_1. (b) The same for dihedral φ vs. improper dihedral χ_2. (c) 3-dimensional free energy surface $F(\varphi, \chi_1, \chi_2)$ from metadynamics projected into the (φ, χ_1)-space. Lines show optimized reaction coordinates. (d) The same but projected into (φ, χ_2)-space (e) Free energy profiles from metadynamics and umbrella sampling, as well as diffusion profiles for optimized reaction coordinates for the cis-to-trans isomerization.

[49]. The paths are parametrized by a path progression parameter σ_s, which can be used as a reaction coordinate in rate theories: $q = \sigma_s$. In total, we optimized four reaction paths: two reaction paths for the transition from cis to trans, each rotating in a different direction, and similarly two reaction paths for the transition from trans to cis (Figure 4c,d). The progress of the optimization is shown in Supporting Information Figure S.6. The optimized reaction coordinates are correlated to χ_1 and χ_2 but do not exhibit any sudden jumps in the two-dimensional distributions (Supporting Information Figures S.7 and S.8).

To employ one-dimensional rate theories on these optimized reaction coordinates, we calculated free energy functions $F(\sigma_s)$, using umbrella sampling and metadynamics, as well as diffusion profiles (see Figure 4e for paths from cis to trans and Figure S.9 in the Supporting Information for paths from trans to cis). We will discuss the rate constant derived from the umbrella sampling for the reaction cis → trans in detail. The rate constants for the reverse reaction have similar values and show the same trends (see Table 2).

For the optimized reaction coordinate, umbrella sampling yields a barrier height of $F^{\ddagger}_{\text{cis}\to\text{trans}} = 98\ \text{kJ mol}^{-1}$, which is $9\ \text{kJ mol}^{-1}$ higher than the free energy barrier for φ. Due to this higher free energy barrier, all one-dimensional rate theories yield lower rates for σ_s than for φ and therefore are in much better agreement with the numerical results. Nonetheless, a discussion of the friction regime is worthwhile.

Despite the increase in the free energy barrier, the energy ratio is only slightly lower than for φ: $RT/F^{\ddagger}_{\text{cis}\to\text{trans}} = 0.025$. By contrast, the friction ratio for σ_s is about ten times higher than for φ : namely, $\xi_{TS}/\omega_{TS} = 5.09$ (for path *cis_trans1*). This is caused by an increased friction coefficient of the effective dynamics and a broader free energy barrier ($\xi_{TS} = 785\ \text{ps}^{-1}$ and $\omega_{TS} = 154\ \text{ps}^{-1}$ for path *cis_trans1*). Consequently, the effective dynamics along $q = \sigma_s$ fall into the high friction regime.

This is also reflected by the values for Kramers' rate constants for the moderate friction regime and for the high friction regime. For $q = \sigma_s$, these two equations yield almost the same value ($k_{\text{cis}\to\text{trans}} = 4.81 \cdot 10^{-5}\ \text{s}^{-1}$ and $k_{\text{cis}\to\text{trans}} = 4.98 \cdot 10^{-5}\ \text{s}^{-1}$, see Table 2), which is only the case in the high friction regime. Another consequence of the higher friction regime is that simple TST considerably overestimates the rate constant ($k_{\text{cis}\to\text{trans}} = 2.57 \cdot 10^{-4}\ \text{s}^{-1}$). Pontryagin's rate theory and the grid-based model yield the same rate constant ($k_{\text{cis}\to\text{trans}} = 3.66 \cdot 10^{-5}\ \text{s}^{-1}$), which is lower than the result from Kramers' rate theory. Since the effective dynamics fall into the high friction regime, this deviation is not likely caused by the assumption of overdamped Langevin dynamics in these theories. The more likely cause is that Kramers' rate theory assumes a position independent diffusion constant, whereas both Pontryagin and grid-based models account for variations in the diffusion constant along the reaction coordinate.

In summary, optimizing the reaction coordinate had two effects on the one-dimensional rate models: the free energy barrier increased, and the friction ratio ξ_{TS}/ω_{TS} increased. Both effects lower the estimate of the rate constant and thus improve the agreement with the simulation results.

3.6 | Umbrella Sampling vs. Metadynamics

For both reaction coordinates, $q = \varphi$ and $q = \sigma_s$, we find that the free energy barriers from metadynamics are consistently 7 to 10 kJ mol^{-1} higher than the free energy barriers from umbrella sampling (Supporting Information Table S.3 and S.4).

Consequently, the rate constants based on metadynamics are about an order of magnitude lower than those based on umbrella sampling.

The sampling for both methods is generous, such that the statistical uncertainty is negligible (Figures 3 and 4e). The free energy functions do not change noticeably when we vary the parameters of the method (force constant and positioning of the umbrella potentials, width of the Gaussian bias potentials in metadynamics, Supporting Information Figure S.11). However, in metadynamics, the error estimated by block analysis [50] as well as the free energy difference between the cis- and the trans-configuration converged only slowly for both reaction coordinates (Supporting Information Figure S.10).

Figure 4 indicates that the optimal reaction coordinate follows a *Z*-shaped curve embedded in multiple collective variables. If the metadynamics bias does not account for all of these relevant collective variables, the system can be pushed into a position parallel to the transition state. However, from this position, the system is unable to transition into state *B*. As a result, repeated failed crossing attempts lead to a buildup of bias in basin *A*, overfilling this minimum. Once the system escapes the local minimum due to the excessive bias, it might not adequately sample the transition state or other important configurations, especially if the metadynamics bias does not account for the slow collective variables necessary for proper exploration. This may ultimately cause an overestimation of the free energy barrier. For a detailed discussion of this effect, see [51], especially Figure 2 therein.

The slow convergence of the error estimates as well as the free energy difference could therefore indicate that further degrees of freedom are relevant to the optimal reaction coordinate. Candidates are the torsion around the neighboring single bonds, that is, C_{12}-C_{13}, and C_{14}-C_{15}. Projecting the configurations into the space spanned by these torsion angles and φ, we find similar "jumps" as in Figure 4, albeit less pronounced (Supporting Information Figure S.12). The optimized reaction coordinate σ_s is still correlated with the torsion around these single bonds, but does not exhibit any sudden jumps in the two-dimensional distributions (Supporting Information Figure S.7), even though these torsion angles were not explicitly part of the optimization process. By comparing Supporting Information Figures S.7 and S.8, we observe that for metadynamics along σ_s, the sampling in the transition state region is clearly reduced compared to umbrella sampling. This supports the conclusion that transitions are more challenging, leading to an overestimation of the free energy barriers.

3.7 | Multidimensional Collective Variables

An alternative to one-dimensional rate theories are grid-based models in multidimensional collective variable spaces. We calculated the three-dimensional free energy function $F(\varphi, \chi_1, \chi_2)$ using metadynamics with three-dimensional Gaussian bias functions, as well as using umbrella sampling with three-dimensional harmonic constraints. The position dependent diffusion profile for the diffusion in each of the three directions were calculated using umbrella sampling with three-dimensional harmonic restraining potentials on a coarse grid (*grid1*) and a fine grid (*grid2*). See Supporting Information Figures S.13 and S.14.

The projection of $F(\varphi, \chi_1, \chi_2)$ into the two-dimensional spaces (φ, χ_1) and (φ, χ_2) are shown in Figure 4c,d, and explain the sudden "jumps" in the two-dimensional distributions in Figure 4a,b. The free energy minima of the cis- and the trans-configuration are slanted in the two-dimensional space. Specifically, the configurations overlap for values of φ near the barrier, and thus φ does not cleanly discriminate between cis- and trans-configuration. In Figure 4c, when going from negative values of φ to positive values across the cis-minimum, χ_1 steadily decreases from $+0.3$ rad to -0.3 rad. At the transition state, the value of χ_1 is restored to $\chi_1 = +0.3$ rad within a short interval of φ, giving rise to "jumps" in the two-dimensional distribution. The correlation of φ to χ_2 shows a similar behavior (Figure 4d). The optimized path follows this sudden change in χ_1 and χ_2 by zigzagging through the three-dimensional space.

To obtain our grid-based rate model, we discretized the three-dimensional space $(\varphi, \chi_1, \chi_2)$, and calculated the rate matrix $\mathbf{Q}$ from the free energy surface and the diffusion profiles using Equation (19), which then yielded the reaction rate constants via Equations (20) and (21). Convergence of the rates with respect to different discretizations of $(\varphi, \chi_1, \chi_2)$ is better for metadynamics than for umbrella sampling (Supporting Information Figure S.1). The rate constants of the three-dimensional models are in good agreement with the rate constants from the simulations (Table 2).

Most importantly, in the three-dimensional models, the results from metadynamics and from umbrella sampling are in excellent agreement. The rate estimates are somewhat sensitive to the model of the diffusion profile. In particular, using a uniform diffusion profile along each of the three collective variables (averaged *grid1* and *grid2*) yields rate constants that are slightly closer to the simulated results than when estimating a fully position dependent diffusion profile (diffusion *grid1* and *grid2*). This might be caused by numerical effects when using the fully position dependent diffusion profile.

We additionally repeated the infrequent metadynamics simulations using three-dimensional Gaussian bias functions in the space spanned by φ, χ_1, and χ_2. The resulting rate constants are very close to those obtained from infrequent metadynamics with one-dimensional biasing (Table 2).

3.8 | Computational Cost

The main computational costs for one-dimensional rate theories (simple TST, Kramers' rate, Pontryagin's rate, and grid-based models) come from the enhanced sampling MD simulations (metadynamics or umbrella sampling), while reweighting to obtain the free energy surface from these simulation data and evaluation of the rate equations exerts a negligible computational cost. Pontryagin's rate and grid-based models additionally require a diffusion profile. When using umbrellas sampling, FES and diffusion profile [27] can be obtained from the same set of simulations. In this case the diffusion profile has negligible computational cost. If metadynamics is used to generate the

FES, additional simulations might be required to estimate the diffusion profiles.

To compare the computational cost of one-dimensional rate theories and grid-based models (Table 3), we therefore focus on the computational cost of MD simulations for generating the FES. For the path-based FES, this cost estimate includes the simulation time for optimizing the four paths (clockwise and counterclockwise rotation for both $k_{\text{cis}\to\text{trans}}$ and $k_{\text{trans}\to\text{cis}}$, total), as well as the simulation time for generating the FES along the optimized paths. We additionally include the computational cost of the MD simulations for infrequent metadynamics, where again the cost of reweighting these trajectories is negligible (Table 3).

Across all methods, the required simulation time ranges between 1 μs and 12 μs. Considering that the mean-first passage time of the cis-trans isomerization (at the present force field) is $\tau = k^{-1} \sim 5\times10^4$ s, this is a remarkably short simulation time. Using enhanced sampling, reweighting, and appropriate rate models, we bridged ten orders of magnitude in time scales from microseconds of total simulation time to hours in molecular process. However, relative to modern computational capabilities, the cost remains significant. At a time step of 2 fs, a simulation time of 1 μs amounts to 500 million force calls, which is currently only feasible for computationally very efficient energy functions.

Since MD simulations for a small molecule in a vacuum with an atomistic force field are relatively inexpensive, we sampled generously without optimizing the simulation times. Therefore, the computational costs presented in Table 3 are not a quantitative benchmark, but should be considered as representative examples.

4 | Computational Methods

4.1 | One-Dimensional Model Systems

The model free energy functions on the circular reaction coordinate $q \in [-\pi, \pi]$ in Figure 1a,b are defined by

$$F(q) = a\cos 2q - b\sin q \tag{24}$$

TABLE 3 | Aggregated MD simulation times to calculate rates for both isomerization directions ($k_{\text{cis}\to\text{trans}}$ and $k_{\text{trans}\to\text{cis}}$).

Method	Reaction Coordinate	Simulation time		Time step
		MetaD	US	
		[10^{-6}s]	[10^{-6}s]	[10^{-15}s]
1D FES	Dihedral φ	2.0	0.996	2.0
1D FES	Path σ	8.0	9.6	1.0
3D FES	Dihedrals			
	φ, χ_1, χ_2	1.0	3.92	2.0
InMetaD		12.0		2.0

in units kJ mol^{-1}. We set $a = 2.4RT$ and $b = -1$ kJ mol^{-1} for Figure 1a, and $a = 10.4\,\beta^{-1}$ kJ mol^{-1} and $b = -1$ kJ mol^{-1} for Figure 1b. The free energy function in Figure 1c was prescribed by a spline interpolation of a metadynamics profile measured along φ of the retinal system studied in this work.

Numerical simulation was carried out by implementing the ISP integrator [52] for underdamped Langevin dynamics (Supporting Information Equation (S.7)) for a particle with effective mass $m = 1$ amu $\cdot$ nm^2 $\cdot$ rad^{-2} and using a time step of $\Delta t = 0.001$ ps. The temperature of the system was $T = 300$ K, and the gas constant $R = 8.314463$ Jmol^{-1}K^{-1} for all simulations. We varied the value of the friction coefficient ξ in ranges that matched the free energy barrier of the model potentials: Figure 1a: $\xi = 0.002$ ps^{-1} to $\xi = 72$ ps^{-1}; Figure 1b: $\xi = 0.005$ ps^{-1} to $\xi = 150$ ps^{-1}; Figure 1c: $\xi = 0.02$ ps^{-1} to $\xi = 713$ ps^{-1}.

For the model systems in Figure 1b,c, we used infrequent metadynamics [24] to enhance the sampling. For Figure 1b, Gaussian bias functions of height 0.1 kJ mol^{-1} and width 0.6 rad were deposited every 300 time steps (weak friction regime); 0.05 kJ mol^{-1} and width 0.4 rad every 150 time steps (moderate and high friction regime). For Figure 1c, Gaussian bias functions of height 0.8 kJ mol^{-1} and width 0.1rad were deposited every 100 time steps (weak friction regime); and of height 0.5 kJ mol^{-1} and width 0.1 rad every 100 time steps (moderate and high friction regime). Well-tempering has been enforced using a biasing factor of 100. Forces were calculated by adding the gradient of the free energy profile to the gradient of the biasing potential $U(q, t)$.

The transition rates in Figure 1a,b were estimated by realizing 100 simulations starting at the left minimum $q_A = -1.6$ rad and measuring the first-passage time to reach the barrier at $q_{TS} = 0$ rad or $q_{TS'} = -\pi$ rad. The reciprocal of the mean and standard deviation of the first-passage times gives the escape rate with its uncertainty. The transition rates in Figure 1b were estimated by the same procedure, but simulations started at $q_A = 0$ rad and stopped at $q_{TS} = 1.6$ rad or $q_{TS'} = -1.6$ rad.

Transition rates for the simple TST formula and Kramers' rate theory in the moderate and high friction limits were calculated by applying the Equations (8), (13), (14), where ω_A, ω_B, or ω_{TS} were calculated from the second derivative of the free energy profile. The integrals in Kramers' rate theory in the weak friction regime (Equation (11)) and Pontryagin's rate theory (Equation (16)) were evaluated by discretizing the interval $[-\pi, +\pi]$ in 100 subsets of equal length and employing the trapezoidal rule. The same discretization was used for the grid-based model (Equation (18)).

4.2 | Atomistic Model of Retinal

Retinal parameters for atomistic force field calculations were taken from DFT studies on the protonated Schiff base [30], adapted to GROMACS format [31], while the connecting amino acid was modeled using the AMBER99SB*-ILDN forcefield [53]. The starting structure was obtained by cutting out the lysine amino acid and retinal cofactor from a recent crystal structure [54]. All simulations are carried out at 300 K

in vacuum using stochastic dynamics with GROMACS [55] version 2019.4 built-in Langevin integrators with a 2 fs step size and an inverse friction coefficient of 2 ps. For the path collective variables, occasionally lower time steps were used. Position restraints of $10,000\ \mathrm{kJ\,mol^{-1}nm^{-2}}$ were put on all heavy atoms of the peptide chain as well as on the lysine chain carbon atoms (Figure 2), while the LINCS constraint algorithm [56] was applied to all hydrogen bonds. Before all simulations, energy minimization and NVT equilibration were performed. Metadynamics [39, 40, 57, 58] and umbrella sampling [43] simulations were carried out by plugging PLUMED [25] with GROMACS. Diffusion profiles were calculated by following Ref [27]. The reaction coordinate was optimized using the PLUMED implementation of the adaptive path CV method in Ref. [49] in combination with metadynamics. Effective masses of the reactant states were calculated by measuring the average squared velocity along the reaction coordinate and applying Equation (7). Frequencies ω_A, ω_B, ω_{TS}, and $\omega_{TS'}$ were calculated from spring constants obtained by harmonically fitting the corresponding wells or barriers. Free energy barriers are measured from the FES directly. One-dimensional rate methods (simple TST, Kramers', Pontryagin) can then be applied straightforwardly. For grid-based methods, 500 cells were used for one-dimensional discretizations, while a discretization of (31,23,23) was used in the 3D CV space (φ, χ_1, χ_2), with χ_1 and χ_2 being discretized in the region between -1 and 1 radians for metadynamics and -0.7 and 0.7 radians for umbrella sampling. Rates from direct numerical simulation were obtained from infrequent metadynamics runs, where acceleration factors were calculated directly by PLUMED. See Supporting Information Section IIA for a complete description of the computational details.

5 | Discussion and Conclusion

Figure 5 summarizes the results of this study. For the thermal cis-trans isomerization in retinal, different methods to calculate the rate constant yield drastically different results. Specifically, reaction-coordinate based rate estimates using the torsion angle $q = \varphi$ as an intuitive reaction coordinate differ by about two orders of magnitude from the infrequent metadynamics results, which is based on counting transitions. Furthermore, within the reaction-coordinate based estimates, the results are very sensitive to the method of calculating the free energy profile: The results with an umbrella sampling FES differ systematically form those with a metadynamic FES.

These deviations are not primarily caused by a poor choice of the friction regime in the Kramers' rate estimates. For $q = \varphi$, the effective dynamics falls into the intermediate friction regime, but using rate equations for overdamped friction instead changes the rate constant only by about a factor of 2. Thus, for a particular choice for calculating $F(q)$, all one-dimensional rate theories yield similar results. The same is true for the optimized reaction coordinate, whose effective dynamics falls into the high friction regime. However, it remains crucial to confirm the friction regime and use the appropriate formula, because Kramers' rate for high friction scenarios may significantly overestimate the rate constant when applied in the wrong friction regime (Figure 1).

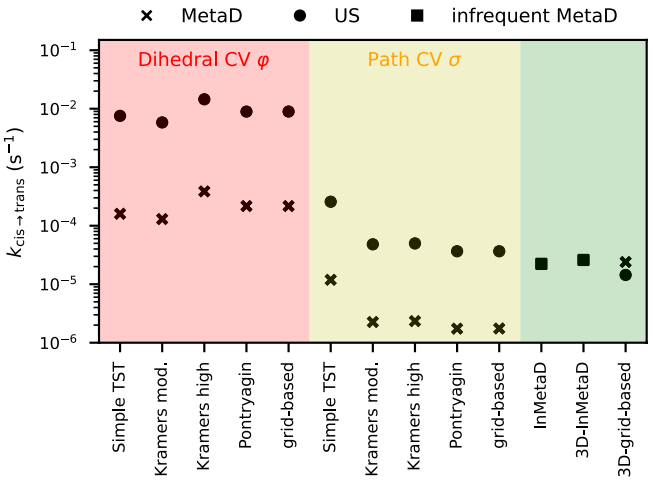

FIGURE 5 | Rate constants determined through different methodologies for the thermal cis-trans isomerization over the $C_{13} = C_{14}$ double bond in retinal.

Optimizing the reaction coordinate lowered the rate estimates of the one-dimensional rate theories by two orders of magnitude compared to $q = \varphi$. These lower rate constants are likely more accurate, since the free energy function of a poor reaction coordinate underestimates the true reaction barrier.

It is surprising at first that, for the cis-trans isomerization, an improved reaction coordinate has such a massive effect on the accuracy of the rate constant. Cis and trans configurations are defined by the torsion angle φ, and therefore $q = \varphi$ cleanly separates reactant and product states [22], which is a crucial criterion for an optimal reaction coordinate. However, the optimization of q revealed that the intuitive reaction coordinate fails another important criterion. In the transition state, the optimized reaction coordinate forms a large angle to the intuitive reaction coordinate $q = \varphi$ (Figure 4c,d). Consequently, the probability flux across the barrier is nearly orthogonal to $q = \varphi$, rather than parallel as expected for an optimal reaction coordinate [22].

This curvature of the optimal reaction coordinate arises, because at the transition state the C_{13} and C_{14} slightly bend out of plane, and thus the reaction coordinate takes a short detour into otherwise rigid degrees of freedom, namely the improper dihedral angles χ_1 and χ_2. This detour is possible because, at the transition state, the electronic structure changes. In this case, the p-orbitals of C_{13} and C_{14} do no longer overlap. This effect is captured by DFT-calculations [2] and reproduced by the empirical force field used in this study.

Since a change in the electronic structure at the transition state is a hallmark of chemical reactions, we suspect that such short detours into orthogonal degrees of freedom (with respect to an intuitive reaction coordinate) will be the rule rather than the exception when modeling chemical reactions. However, finding such a curved optimal reaction coordinate is not trivial, even if an initial reaction coordinate and candidates for further correlated degrees of freedom are known, as in the case of retinal [2, 48]. Besides the path-based method [49] we used in our study, a wide range of other methods to identify optimal reaction

coordinates have been proposed [59–61], including recent approaches based on neural networks [62, 63].

An alternative to optimizing the reaction coordinate is to improve the estimate of the rate constant for a sub-optimal reaction coordinate q by including non-Markovian effects into the effective dynamics along q. The corresponding equations are based on the generalized Langevin equation (GLE). Here, non-Markovian behavior arises from the memory kernel, which is a time-integral over the time-dependent friction coefficient [64–66]. Memory kernels are notoriously hard to predict, but recently multiple methods have emerged to model them [67–69]. In addition, Grote–Hynes theory provides an equation for the memory kernel [8]. The resulting rate equation has the same functional form as Kramers rate equation for the moderate friction regime (Equation (13)), where the Markovian friction ξ is replaced by the Laplace transform of the time-dependent friction coefficient [13]. In general, the closer the reaction coordinate follows the probability flux of the reaction, the smaller are the non-Markovian effects [65]. Although non-Markovian rate theories provide accurate rate estimates even for imperfect reaction coordinates, using these suboptimal reaction coordinates risks obscuring important mechanistic details needed for understanding the reaction. For example in retinal, the out-of-plane bending of C_{13} and C_{14} near the transition state is not captured by the initial reaction coordinate $q = \varphi$.

For our system, despite using an optimized reaction coordinate, metadynamics and umbrella sampling produced different free energy barriers, leading to significantly different rate estimates, as shown in Figure 5. This is likely caused by the strong curvature of the optimized reaction coordinate and might indicate that $q = \sigma_s$ is not yet fully optimal.

Grid-based models in a multidimensional collective variable space offer an alternative to optimizing the one-dimensional reaction coordinate or including memory effects. Using the torsion angle φ and two improper torsion angles at C_{13} and C_{14} as collective variables, we obtained rate estimates that are in very good agreement with the simulation results (Figure 5). Moreover, for these multidimensional models, the free energy functions derived from metadynamics and umbrella sampling agree, leading to similar rate constants. Multidimensional models have additional advantages: they can be applied to multistate dynamics, do not assume timescale separation, and they yield information on all of the slow processes in the system [33, 34]. The trade-off is the need to estimate a multidimensional free energy surface.

Furthermore, methods that model the reaction rate by envisioning a flux over a dividing surface [70] rather than a maximum in an energy landscape can be considered. In variational transition state theory (VTST), different approaches are used to optimize the dividing surface and minimize the TST reaction rate [6, 7, 71]. The reactive flux method [72], links the flux across a dividing surface to a correlation function which can be estimated from molecular simulations. Modern methods based on this framework include transition path sampling [22, 73], transition interface sampling [74] and forward flux sampling [75].

Our results show that rate constants for chemical reactions can be determined with high accuracy (within the classical approximation) from molecular simulations. The caveat is that the methods need to be carefully chosen for the system at hand. Of the various parameters that influence the rate constant, the curvature of the reaction coordinate at the transition state emerges as the most critical one.

Acknowledgments

This research has been funded by Deutsche Forschungsgemeinschaft (DFG) through grant SFB 1114 "Scaling Cascades in Complex Systems"–project number 235221301, as well as by the Cluster of Excellence MATH+, project AA1-15 "Math-powered drug-design". S.G. acknowledges funding by the Deutsche Forschungsgemeinschaft (DFG, German Research Foundation) under Germany´s Excellence Strategy – EXC 2008 – 390540038 – UniSysCat. Open Access funding enabled and organized by Projekt DEAL.

Data Availability Statement

The data that support the findings of this study are available from the corresponding author upon reasonable request.

References

1. F. Vitalini, A. S. Mey, F. Noé, and B. G. Keller, "Dynamic Properties of Force Fields," *Journal of Chemical Physics* 142, no. 8 (2015): 084101.

2. S. Ghysbrecht and B. G. Keller, "Thermal Isomerization Rates in Retinal Analogues Using Ab-Initio Molecular Dynamics," *Journal of Computational Chemistry* 45, no. 16 (2024): 1390–1403.

3. J. N. Harvey, F. Himo, F. Maseras, and L. Perrin, "Scope and Challenge of Computational Methods for Studying Mechanism and Reactivity in Homogeneous Catalysis," *ACS Catalysis* 9, no. 8 (2019): 6803–6813.

4. D. Marx and J. Hutter, "Ab Initio Molecular Dynamics: Theory and Implementation," *Modern Methods and Algorithms of Quantum Chemistry NIC Series* 1 (2000): 301–449.

5. H. Eyring, "The Activated Complex in Chemical Reactions," *Journal of Chemical Physics* 3, no. 2 (1935): 107–115.

6. J. C. Keck, "Variational Theory of Chemical Reaction Rates Applied to Three-Body Recombinations," *Journal of Chemical Physics* 32, no. 4 (1960): 1035–1050.

7. D. G. Truhlar and B. C. Garrett, "Variational Transition-State Theory," *Accounts of Chemical Research* 13, no. 12 (1980): 440–448.

8. R. F. Grote and J. T. Hynes, "The Stable States Picture of Chemical Reactions. II. Rate Constants for Condensed and Gas Phase Reaction Models," *Journal of Chemical Physics* 73, no. 6 (1980): 2715–2732.

9. R. Schade, T. Kenter, H. Elgabarty, M. Lass, T. D. Kühne, and C. Plessl, "Breaking the Exascale Barrier for the Electronic Structure Problem in Ab-Initio Molecular Dynamics," *International Journal of High Performance Computing Applications* 37, no. 5 (2023): 530–538.

10. M. Gaus, Q. Cui, and M. Elstner, "DFTB3: Extension of the Self-Consistent-Charge Density-Functional Tight-Binding Method (SCC-DFTB)," *Journal of Chemical Theory and Computation* 7, no. 4 (2011): 931–948.

11. E. Kocer, T. W. Ko, and J. Behler, "Neural Network Potentials: A Concise Overview of Methods," *Annual Review of Physical Chemistry* 73 (2022): 163–186.

12. F. Noé, A. Tkatchenko, K.-R. Müller, and C. Clementi, "Machine Learning for Molecular Simulation," *Annual Review of Physical Chemistry* 71 (2020): 361–390.

13. B. Peters, *Reaction Rate Theory and Rare Events*, 1st ed. (Amsterdam: Elsevier, 2017).

14. F. Pietrucci, "Strategies for the Exploration of Free Energy Landscapes: Unity in Diversity and Challenges Ahead," *ReViP* 2 (2017): 32–45.

15. M. Salvalaglio, P. Tiwary, and M. Parrinello, "Assessing the Reliability of the Dynamics Reconstructed From Metadynamics," *Journal of Chemical Theory and Computation* 10, no. 4 (2014): 1420–1425.

16. T. J. Lane, D. Shukla, K. A. Beauchamp, and V. S. Pande, "To Milliseconds and Beyond: Challenges in the Simulation of Protein Folding," *Current Opinion in Structural Biology* 23, no. 1 (2013): 58–65.

17. K. Ahmad, A. Rizzi, R. Capelli, D. Mandelli, W. Lyu, and P. Carloni, "Enhanced-Sampling Simulations for the Estimation of Ligand Binding Kinetics: Current Status and Perspective," *Frontiers in Molecular Biosciences* 9 (2022): 899805.

18. A. Arjun and P. Bolhuis, "Molecular Understanding of Homogeneous Nucleation of CO2 Hydrates Using Transition Path Sampling," *Journal of Physical Chemistry B* 125, no. 1 (2020): 338–349.

19. W. T. Borden, "Reactions That Involve Tunneling by Carbon and the Role That Calculations Have Played in Their Study," *Wiley Interdisciplinary Reviews: Computational Molecular Science* 6, no. 1 (2016): 20–46.

20. Y. Zhang, Y. Wang, X. Xu, Z. Chen, and Y. Yang, "Vibrational Spectra of Highly Anharmonic Water Clusters: Molecular Dynamics and Harmonic Analysis Revisited With Constrained Nuclear-Electronic Orbital Methods," *Journal of Chemical Theory and Computation* 19, no. 24 (2023): 9358–9368.

21. S. Kieninger, L. Donati, and B. G. Keller, "Dynamical Reweighting Methods for Markov Models," *Current Opinion in Structural Biology* 61 (2020): 124–131.

22. P. G. Bolhuis, D. Chandler, C. Dellago, and P. L. Geissler, "Transition Path Sampling: Throwing Ropes Over Rough Mountain Passes, in the Dark," *Annual Review of Physical Chemistry* 53, no. 1 (2002): 291–318.

23. D. M. Zuckerman and L. T. Chong, "Weighted Ensemble Simulation: Review of Methodology, Applications, and Software," *Annual Review of Biophysics* 46 (2017): 43–57.

24. P. Tiwary and M. Parrinello, "From Metadynamics to Dynamics," *Physical Review Letters* 111, no. 23 (2013): 230602.

25. G. A. Tribello, M. Bonomi, D. Branduardi, C. Camilloni, and G. Bussi, "PLUMED 2: New Feathers for an Old Bird," *Computer Physics Communications* 185, no. 2 (2014): 604–613.

26. J. O. Daldrop, J. Kappler, F. N. Brünig, and R. R. Netz, "Butane Dihedral Angle Dynamics in Water Is Dominated by Internal Friction," *PNAS* 115, no. 20 (2018): 5169–5174.

27. G. Hummer, "Position-Dependent Diffusion Coefficients and Free Energies From Bayesian Analysis of Equilibrium and Replica Molecular Dynamics Simulations," *New Journal de Physique* 7, no. 1 (2005): 34.

28. H. A. Kramers, "Brownian Motion in a Field of Force and the Diffusion Model of Chemical Reactions," *Physica* 7, no. 4 (1940): 284–304.

29. P. Hänggi, P. Talkner, and M. Borkovec, "Reaction-Rate Theory: Fifty Years After Kramers," *Reviews of Modern Physics* 62 (1990): 251–341.

30. S. Hayashi, E. Tajkhorshid, and K. Schulten, "Structural Changes During the Formation of Early Intermediates in the Bacteriorhodopsin Photocycle," *Biophysical Journal* 83, no. 3 (2002): 1281–1297.

31. E. Malmerberg, Z. Omran, J. S. Hub, et al., "Time-Resolved WAXS Reveals Accelerated Conformational Changes in Iodoretinal-Substituted Proteorhodopsin," *Biophysical Journal* 101, no. 6 (2011): 1345–1353.

32. L. Pontryagin, A. Andronov, and A. Vitt, "On the Statistical Investigation of Dynamic Systems," *Zhurnal Eksperimental'noi i Teoreticheskoi Fiziki* 3 (1933): 165.

33. H. C. Lie, K. Fackeldey, and M. Weber, "A Square Root Approximation of Transition Rates for a Markov State Model," *SIAM Journal on Matrix Analysis and Applications* 34 (2013): 738–756.

34. L. Donati, M. Weber, and B. G. Keller, "Markov Models From the Square Root Approximation of the Fokker–Planck Equation: Calculating the Grid-Dependent Flux," *Journal of Physics. Condensed Matter* 33, no. 11 (2021): 115902.

35. D. J. Bicout and A. Szabo, "Electron Transfer Reaction Dynamics in Non-Debye Solvents," *Journal of Chemical Physics* 109 (1998): 2325–2338, https://doi.org/10.1063/1.476800.

36. M. Heida, M. Kantner, and A. Stephan, "Consistency and Convergence for a Family of Finite Volume Discretizations of the Fokker–Planck Operator," *ESAIM. Mathematical Modelling and Numerical Analysis* 55, no. 6 (2021): 3017–3042.

37. A. M. Berezhkovskii and A. Szabo, "Committors, First-Passage Times, Fluxes, Markov States, Milestones, and All That," *Journal of Chemical Physics* 150, no. 5 (2019): 054106.

38. A. Barducci, G. Bussi, and M. Parrinello, "Well-Tempered Metadynamics: A Smoothly Converging and Tunable Free-Energy Method," *Physical Review Letters* 100, no. 2 (2008): 020603.

39. H. Grubmüller, "Predicting Slow Structural Transitions in Macromolecular Systems: Conformational Flooding," *Physical Review E* 52, no. 3 (1995): 2893.

40. A. F. Voter, "Hyperdynamics: Accelerated Molecular Dynamics of Infrequent Events," *Physical Review Letters* 78, no. 20 (1997): 3908.

41. P. Tiwary and B. Berne, "Kramers Turnover: From Energy Diffusion to Spatial Diffusion Using Metadynamics," *Journal of Chemical Physics* 144, no. 13 (2016): 134103.

42. K. Schulten and S. Hayashi, "Quantum biology of retinal," *in Quantum Effects in Biology*, eds. M. Mohseni, Y. Omar, G. S. Engel, and M. B. Plenio (Cambridge: Cambridge University Press, 2014), 237–263.

43. G. M. Torrie and J. P. Valleau, "Nonphysical Sampling Distributions in Monte Carlo Free-Energy Estimation: Umbrella Sampling," *Journal of Computational Physics* 23, no. 2 (1977): 187–199.

44. S. Kumar, J. M. Rosenberg, D. Bouzida, R. H. Swendsen, and P. A. Kollman, "The Weighted Histogram Analysis Method for Free-Energy Calculations on Biomolecules. I. The Method," *Journal of Computational Chemistry* 13, no. 8 (1992): 1011–1021.

45. B. M. Dickson, "Erroneous Rates and False Statistical Confirmations From Infrequent Metadynamics and Other Equivalent Violations of the Hyperdynamics Paradigm," *Journal of Chemical Theory and Computation* 15, no. 1 (2018): 78–83.

46. S. A. Khan, B. M. Dickson, and B. Peters, "How Fluxional Reactants Limit the Accuracy/Efficiency of Infrequent Metadynamics," *Journal of Chemical Physics* 153, no. 5 (2020): 054125.

47. B. Peters, "Reaction Coordinates and Mechanistic Hypothesis Tests," *Annual Review of Physical Chemistry* 67 (2016): 669–690.

48. A.-N. Bondar, M. Knapp-Mohammady, S. Suhai, S. Fischer, and J. C. Smith, "Ground-State Properties of the Retinal Molecule: From Quantum Mechanical to Classical Mechanical Computations of Retinal Proteins," *Theoretical Chemistry Accounts* 130 (2011): 1169–1183.

49. G. D. Leines and B. Ensing, "Path Finding on High-Dimensional Free Energy Landscapes," *Physical Review Letters* 109, no. 2 (2012): 020601.

50. G. Bussi and G. Tribello, "Analyzing and Biasing Simulations with PLUMED," in *Biomolecular Simulations. Methods in Molecular Biology*, eds. M. Bonomi and C. Camilloni (New York, NY: Springer, 2019), 529–578.

51. A. Laio and F. L. Gervasio, "Metadynamics: A Method to Simulate Rare Events and Reconstruct the Free Energy in Biophysics, Chemistry

and Material Science," *Reports on Progress in Physics* 71, no. 12 (2008): 126601.

52. J. A. Izaguirre, C. R. Schweet, and V. Pande, "Multiscale Dynamics of Macromolecules Using Normal Mode Langevin," *Pacific Symposium on Biocomputing* 15 (2010): 240–251.

53. K. Lindorff-Larsen, S. Piana, K. Palmo, et al., "Improved Side-Chain Torsion Potentials for the Amber FF99SB Protein Force Field," *Proteins: Structure, Function, and Bioinformatics* 78, no. 8 (2010): 1950–1958.

54. O. Volkov, K. Kovalev, V. Polovinkin, et al., "Structural Insights Into Ion Conduction by Channelrhodopsin 2," *Science* 358, no. 6366 (2017).

55. M. J. Abraham, T. Murtola, R. Schulz, et al., "GROMACS: High Performance Molecular Simulations Through Multi-Level Parallelism From Laptops to Supercomputers," *SoftwareX* 1 (2015): 19–25.

56. B. Hess, H. Bekker, H. J. Berendsen, and J. G. Fraaije, "LINCS: A Linear Constraint Solver for Molecular Simulations," *Journal of Computational Chemistry* 18, no. 12 (1997): 1463–1472.

57. T. Huber, A. E. Torda, and W. F. Van Gunsteren, "Local Elevation: A Method for Improving the Searching Properties of Molecular Dynamics Simulation," *Journal of Computer-Aided Molecular Design* 8 (1994): 695–708.

58. A. Laio and M. Parrinello, "Escaping Free-Energy Minima," *PNAS* 99, no. 20 (2002): 12562–12566.

59. E. Weinan and E. Vanden-Eijnden, "Transition-Path Theory and Path-Finding Algorithms for the Study of Rare Events," *Annual Review of Physical Chemistry* 61 (2010): 391–420.

60. B. Roux, "String Method With Swarms-of-Trajectories, Mean Drifts, Lag Time, and Committor," *Journal of Physical Chemistry A* 125, no. 34 (2021): 7558–7571.

61. K. Palacio-Rodriguez and F. Pietrucci, "Free Energy Landscapes, Diffusion Coefficients, and Kinetic Rates From Transition Paths," *Journal of Chemical Theory and Computation* 18, no. 8 (2022): 4639–4648.

62. K. Shmilovich and A. L. Ferguson, "Girsanov Reweighting Enhanced Sampling Technique (GREST): On-The-Fly Data-Driven Discovery of and Enhanced Sampling in Slow Collective Variables," *Journal of Physical Chemistry A* 127, no. 15 (2023): 3497–3517.

63. H. Jung, R. Covino, A. Arjun, et al., "Machine-Guided Path Sampling to Discover Mechanisms of Molecular Self-Organization," *Nature Computational Science* 3 (2023): 1–12.

64. H. Mori, "Transport, Collective Motion, and Brownian Motion," *Progress in Theoretical Physics* 33, no. 3 (1965): 423–455.

65. R. Zwanzig, "Memory Effects in Irreversible Thermodynamics," *Physics Review* 124, no. 4 (1961): 983.

66. R. Zwanzig, *Nonequilibrium Statistical Mechanics* (New York: Oxford University Press, 2001).

67. A. J. Dominic, III, S. Cao, A. Montoya-Castillo, and X. Huang, "Memory Unlocks the Future of Biomolecular Dynamics: Transformative Tools to Uncover Physical Insights Accurately and Efficiently," *Journal of the American Chemical Society* 145, no. 18 (2023): 9916–9927.

68. H. Vroylandt, L. Goudenège, P. Monmarché, F. Pietrucci, and B. Rotenberg, "Likelihood-Based Non-Markovian Models From Molecular Dynamics," *PNAS* 119, no. 13 (2022): e2117586119.

69. C. Ayaz, L. Tepper, F. N. Brünig, J. Kappler, J. O. Daldrop, and R. R. Netz, "Non-Markovian Modeling of Protein Folding," *PNAS* 118, no. 31 (2021): e2023856118.

70. E. Wigner, "The Transition State Method," *Transactions of the Faraday Society* 34 (1938): 29–41.

71. J. L. Bao and D. G. Truhlar, "Variational Transition State Theory: Theoretical Framework and Recent Developments," *Chemical Society Reviews* 46, no. 24 (2017): 7548–7596.

72. D. Chandler, "Statistical Mechanics of Isomerization Dynamics in Liquids and the Transition State Approximation," *Journal of Chemical Physics* 68, no. 6 (1978): 2959–2970.

73. C. Dellago, P. G. Bolhuis, and D. Chandler, "On the Calculation of Reaction Rate Constants in the Transition Path Ensemble," *Journal of Chemical Physics* 110, no. 14 (1999): 6617–6625.

74. T. S. Van Erp, D. Moroni, and P. G. Bolhuis, "A Novel Path Sampling Method for the Calculation of Rate Constants," *Journal of Chemical Physics* 118, no. 17 (2003): 7762–7774.

75. R. J. Allen, D. Frenkel, and P. R. Ten Wolde, "Forward Flux Sampling-Type Schemes for Simulating Rare Events: Efficiency Analysis," *Journal of Chemical Physics* 124, no. 19 (2006): 194111.

Supporting Information

Additional supporting information can be found online in the Supporting Information section.